Available online at www.sciencedirect.com

ScienceDirect

Procedia Manufacturing 26 (2018) 595–606

Procedia MANUFACTURING

www.elsevier.com/locate/procedia

46th SME North American Manufacturing Research Conference, NAMRC 46, Texas, USA

Machining behavior of additively manufactured and cast-wrought nickel-based superalloy (IN 625)

Rajesh Kumar Ananda-Kumar[a], Wilfredo Moscoso-Kingsley[a], Gregor Jacob[b], Alkan Donmez[b], Viswanathan Madhavan[a]*

[a]*Wichita State University, 1845 Fairmount St, Wichita 67260, USA*
[b]*National Institute of Standards and Technology, 100 Bureau Dr , Gaithersburg 20899, USA*

* Corresponding author. Tel.: +1-316-978-5913; fax: +1-316-978-3742
E-mail address: vis.madhavan@wichita.edu

Abstract

Additively manufactured (AM) and cast-wrought (CW) nickel-based superalloy (IN 625) with known processing history and quasi-static properties have been investigated for their relative machinability, in terms of tool temperature and wear, as well as machining force and chip morphology. Transparent cutting tools were used to cut tubular specimens of both materials. Visible and near infrared radiation emitted by the chip-tool interface was measured through the transparent tool using an image intensified CCD camera. A calibration procedure was used to convert this into apparent blackbody temperature from which the true temperature was inferred using literature values of emissivity of polished IN 625. Machining forces along the cutting and thrust force directions were measured using a dynamometer. Tool wear and chip morphology were characterized by measurement of tool volume loss and by scanning the chip upper side, using a 3D profilometer. It was found that during machining, AM IN 625 behaves differently from CW IN 625 of similar chemical composition. Significant differences in tool temperature, tool wear, and chip formation mechanisms were observed.

© 2018 The Authors. Published by Elsevier B.V.
Peer-review under responsibility of the scientific committee of the 46th SME North American Manufacturing Research Conference.

Keywords: hybrid; additive; subtractive; machinability; temperature; wear.

1. Introduction

Hybrid manufacturing processes combining additive manufacturing (AM) and subtractive manufacturing (SM) have emerged as potentially viable processes to obtain fully functional parts with acceptable mechanical properties, dimensional accuracy and surface integrity [1]. Although AM by

2351-9789 © 2018 The Authors. Published by Elsevier B.V.
Peer-review under responsibility of the scientific committee of the 46th SME North American Manufacturing Research Conference.
10.1016/j.promfg.2018.07.070

itself offers access to complex geometries and efficient material utilization, it is handicapped by dimensional accuracy and surface integrity [1]. The poor dimensional accuracy and surface integrity resulting from AM processing demands finishing by subtractive routes such as machining.

There are some instances that indicate that AM materials can be produced, after proper heat treatments, with mechanical properties often superior to those of the conventional, cast and wrought counterparts [2]. Due to rapid cooling of the small volumes locally heated, the microstructure of the AM material may be ultra-refined, and therefore its strength may be larger than that of the conventional material [3]. Many other reports, however, indicate the contrary. The properties obtained from AM processing strongly depend on process inputs. In general, AM materials have mechanical properties that are distinct from those of conventional materials.

Jacob et al. [4] observed the mechanical strength and ductility of AM stainless steel (17-4 PH) as a function of source powder recycling. The results were the same when recycling the source powder up to ten times. The as-built AM steel had higher yield strength and lower ductility (1 344 MPa and 26 %, respectively) than those from American Society for Testing and Materials-compliant cast-wrought counterparts (1 034 MPa and 40 %, respectively). The report attributes the results to the presence of a nearly fully martensitic microstructure in the AM material. Whereas Rafi et al. [5] showed that AM 17-4 PH stainless steel resulted in low strength and high ductility compared to a solution treated cast-wrought control sample, their microstructural analysis revealed that they had not been successful at producing a fully martensitic phase directly from the melt re-solidification. Mower et al. [3] studied the static and dynamic mechanical behavior of several materials processed by AM routes. For most of the materials tested the tensile strength obtained directly from the printing was either lower or comparable to those from cast-wrought counterparts. However, the 316L steel that was synthesized had tensile strength of approximately 699 MPa, which was higher than that of the cast-wrought equivalent of approximately 563 MPa. Elongation at failure was the same for both materials (approximately 28 % to 30 %). Fatigue strength was generally lower in the AM material than in the conventional material. Although hot isostatic pressing (HIP) increased fatigue strength, the fatigue performance of the AM material was generally inferior to that of the conventional material. Hollander et al. [6] reported the mechanical properties of AM Ti-6Al-4V and conventional Ti-6Al-4V. Their report shows tensile strength and elongation at breakage of approximately 1 211 MPa and 6.5 %, respectively, for the as-built AM material, and approximately 1 042 MPa and 13 %, respectively, for the cast-wrought counterpart.

The unique mechanical properties of AM materials may have a negative impact on their machinability, and thus may challenge SM processing to obtain dimensional accuracy and surface integrity. An extra layer of complications faced by SM post-processing may arise from the significant strength anisotropy also observed in materials processed by AM routes [7], which is associated with directional solidification and columnar grain growth.

The complications that may arise during the machining of additively printed parts may be particularly adverse for parts made from superalloys of titanium or nickel. As a result of the high strength and low heat capacity of these alloys, machining materials such as Ti6Al4V and IN 718 results in high tool temperatures and wear rates [8]. In addition, the low thermal conductivity of these materials promotes adiabatic heating during their machining, which not only feeds back into the tool temperature and wear rate, but plays a role in the type of chip formation (continuous vs. serrated), and in the machining dynamics [9].

The machinability of a material is affected by a number of factors including machining force, chip formation mechanism, chip-tool contact friction, subsurface thermo-mechanical damage; and ultimately tool temperature and wear [10]. Control of temperature and wear at the tool rake face, where they are usually most severe, is particularly elusive. Since temperature and wear are intrinsically related, their control can only proceed after precise temperature measurement. Attempts to measure the temperature at the chip-tool interface have relied on methods such as (1) the tool-workpiece thermocouple technique [11, 12], (2) correlation of metallurgical changes in the tool material and temperature [13, 14], (3) implantation of micro-thermocouple arrays on the tool rake face [8], and (4) through-the-tool thermography [15, 16, 17]. Out of these methods, through-the-tool thermography offers low uncertainty, and high spatial and temporal resolution; and the observations are made directly on the tool rake face. The technique's uncertainty decreases with increase in the temperature of the target (the chip-tool interface), and is quite low (±10 °C) at approximately 1 000 °C [18], which is the expected temperature of the chip-tool interface when machining superalloys. Therefore, the use of thermography to measure the temperature at the chip-tool interface is especially attractive for the machining of superalloys.

This paper provides an evaluation of the machinability of nickel-based superalloy (IN 625) prepared by an AM route (AM IN 625). The material, originally in the form of hollow cylinders, was prepared by a laser powder bed fusion (LPBF) process available at the National Institute of Standards and Technology (NIST), and after the preparation it was subject to machining tests. The machining was performed by cutting the cylinders along the direction transverse to the LPBF build direction, as in axial turning. The machining force (cutting and thrust forces), and the temperature of the chip-tool interface were observed *in situ*. Tool wear and chip morphology were observed *ex situ*. These parameters were compared to those obtained from the machining of a conventional, cast-wrought IN 625 (CW IN 625). The AM IN 625 had the following properties: elastic modulus = 179 GPa, yield stress = 780 MPa, ultimate tensile strength = 1.05 GPa, and elongation at break = 36 %. The CW IN 625 had the following properties: elastic modulus = 205 GPa, yield stress = 490 MPa, ultimate tensile strength = 0.93 GPa, and elongation at break = 52 %. Since the CW IN 625 material had been subject to an annealing heat treatment at 1 038 °C for a short amount of time (unknown), both the AM and CW workpieces were subject to the same treatment at 1 038 °C for 5 min, in air, and then air cooled. The short time was justified because the workpieces were of small wall thickness (0.9 mm), so they would have reached the target temperature in negligible time, thus minimizing grain growth. The heat treatments were performed after turning the workpieces into final shape, and prior to machining experiments. It must be noted that complete characterization of the materials, after the annealing process, is being performed and will be reported in the future.

The machining was performed with a specially designed tool, but some tests were also performed with a commercially available tungsten carbide (WC) tool. The specially designed tool, a transparent yttrium aluminum garnet (YAG) cube with 12 useable cutting edges, provided an optical path to the interface for the observation of the radiation emitted by the chip underside. This tool was utilized for all the experiments shown herein, except a few tests that were performed with the WC tool. Unless otherwise noted, the YAG tool was used. The radiation was converted into real chip-tool interface temperature after a calibration procedure. The comparisons show clear differences in chip formation mechanisms for AM and CW IN 625, and in the chip-tool interface temperature.

2. Experimental Configuration

The temperature distribution at the chip-tool interface was obtained after machining on a high-rigidity and high-speed, custom-built lathe. The setup was designed to rotate the workpiece and feed it towards the stationary tool as in axial turning (Fig. 1). The lathe’s loop stiffness was on the order of 100 N/µm. The spindle speed capacity was 1 046.7 rad/s. Unless otherwise noted, the cutting tool was made of an optically transparent YAG crystal. The transparent tool and the mirror mounted under it (Fig. 1, inset) enabled direct observation of the chip-tool interface, which was performed with an intensified charged couple device (ICCD) camera[1].

The YAG tools were 6 mm cubes having 12 usable cutting edges. To increase the toughness of the YAG cubes, they were annealed by heating them at 4 °C per minute to 1 600 °C, held there for 10 hours, and cooled back to ambient temperature at 4 °C per minute. The edge radius was 2.5 µm. The YAG cubes were held by a specially designed tool holder that allowed cutting at -5° rake angle and +5° relief angle. The fixture supported the cubes on three mutually orthogonal faces. A clamp secured the cubes in place. The tool holder had a small pocket under the cube support, where a 1.1 mm thick first-surface mirror was mounted. As mentioned above, the mirror directed the radiation emitted by the surface of the chip in contact with the tool rake face towards the camera. A commercial tungsten carbide (WC) tool with rake angle = 5° and relief angle = 6° was also used for some tests.

---

[1] Princeton Instruments PI-MAX2:1003HBf with thrid generation HB filmless intensifier and P46 phosphor.

The workpieces were prepared by machining either from the AM hollow cylinders or from commercially sourced cylindrical rods. The workpieces were tubes having 20.1 mm outer diameter (OD) and 0.9 mm wall thickness. The tubes were held by a collet on the lathe that allowed a firm installation with minimal runout. The experimental configuration approximated orthogonal cutting. The cutting speed was varied between 1 m/s and 4 m/s.

The ICCD camera was coupled to a custom-built lens that incorporated a series of apertures (an aperture stop, a field stop and a Lyot stop), designed to mitigate size-of-source effects [19]. The imaging system had an effective magnification of 5x, and a focal plane array (FPA) of 1 024 pixels by 1 024 pixels. The pixels were squares having 12.8 µm long sides. Therefore, each pixel was equivalent to approximately a square region of the chip-tool interface having 2.56 µm sides. The total field of view was a square of area = 2 621 µm x 2 621 µm. The camera control software allowed grouping several pixels into one box—a technique known as "binning"— to increase the frame rate, which after binning was 25 Hz. Binning combined 16 pixels in a 4 pixel by 4 pixel square sub-array into one pixel. In other words, the 1 024 pixel by 1 024 pixel array was converted into a 1 024/4 x 1 024/4 = 256 pixel by 256 pixel array. Each bin of pixels was then equivalent to a 10.24 µm x 10.24 µm area of the chip-tool interface. Therefore, the theoretical spatial resolution of the imaging system was about 20 µm.

The experiments produced chip-tool contact lengths, measured from the cutting edge, along the rake face, of between 100 µm and 150 µm. Along this length, the field included about 10 to 15 observation points. The images were obtained at a frame rate of 25 Hz. The camera had a 16-bit dynamic range, which means that the maximum radiation intensity it could detect, in counts, was 65 535. The laboratory was darkened throughout the experiments to reduce background light. The camera was used to record the background prior to each cutting experiment. The mean background image was obtained from a number of frames, after computing average counts, pixel by pixel. The mean background image was subtracted from all frames taken during machining, pixel by pixel. Typical background images had, across all pixels, a mean intensity of ≈ 250 counts, with a standard deviation of ≈ 6 counts.

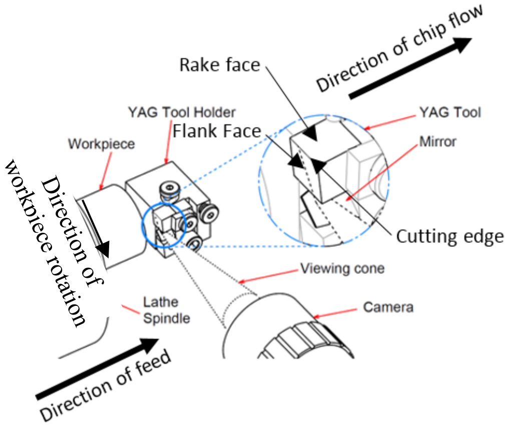

Fig. 1. Schematic of the experimental setup for through-the-tool temperature measurement.

To relate measured radiation intensity to chip-tool interface temperature two pieces of information are needed: 1) The relation between the radiation intensity read by the ICCD camera and the radiance of a blackbody of known temperature (i.e., the calibration), and 2) the emissivity of the side of the chip in contact with the tool rake face (i.e., the emissivity of the chip underside). The calibration was performed by recording images of the cavity of a blackbody source, after heating and cooling it through temperatures ranging from 700 °C to 982 °C. As with the actual machining experiments, the camera was used to record the background light noise prior to each calibration experiment. The mean background image was subtracted from all frames taken during the calibration, pixel by pixel. The emissivity was estimated from information compiled from [20], which reported that the emissivity (ε) of IN 625 for non-oxidized and smooth surfaces (as the chip underside) is approximately 0.3. Thus, the emissivity used herein was 0.3.

The radiation intensity from the blackbody, after background noise removal, was measured for a range of camera exposure times. The measured data suggests that, for a source at a given temperature, the radiation intensity per unit exposure time was nearly a constant. This fact enabled the use of a single calibration curve to relate radiation intensity and temperature for all exposure time values. The camera responded to the radiation with minimal hysteresis (< 0.5 %), so there is no bias in reading increasing or decreasing temperatures. The calibration was obtained by fitting the data for blackbody radiation intensity vs. temperature to the forward Sakuma-Hattori equation [21, 22]. The equation has the following form:

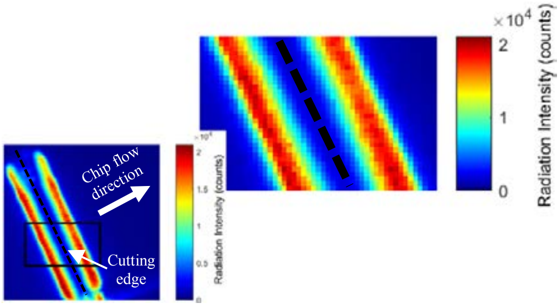

Fig. 2. A sample image of the radiation intensity field of the tool rake face, as measured by the camera. The right image is a magnified view of the region in the black rectangle on the left image.

$$F(T) = \frac{C}{\exp\left(\frac{c_2}{AT + B}\right) - 1} \qquad (1)$$

where, $F(T)$ is the radiation intensity from the blackbody (counts), T is the blackbody temperature (K), c_2 is the second radiation constant (14 388 µm K), and C, and A and B are calibration constants. The fit values are C = 5.15E+14 counts, and A = 0.4 µm and B = 135 µm K. The Sakuma-Hattori equation fits the data with a goodness of fit of over 0.999 (coefficient of determination, on a scale from 0 to 1). Corrections for radiation loss through the YAG tool are made, and the Sakuma-Hattori equation is inverted to calculate temperature for a given radiation intensity. The correction involves an estimation of the radiation loss through the YAG for the effective wavelength of the imaging system, which is given by:

$$\lambda_{eff} = A + B/T \qquad (2)$$

At the expected temperature of approximately 1 250 K the effective wavelength is approximately 0.5 µm. At this wavelength, the transmissivity of YAG is approximately 0.8, as per datasheet from the YAG supplier. Thus, the loss factor (LF) can be taken as approximately 0.2.

After initial trials, it was determined that the machining would produce sufficient signal to noise ratio without saturation for an exposure time of 0.1 ms, 0.5 ms, and 2 ms, for cutting speeds of 3 m/s, 2 m/s, and 1 m/s, respectively.

The lathe feed was controlled by a feedback controller. The control software generated a voltage signal that was used to initiate lathe feed and to trigger image acquisition. Therefore, lathe feed and image acquisition started simultaneously. To position the workpiece at a constant distance from the tool without making it contact the cutting edge, the workpiece was brought towards the tool until a precision-made plastic shim carefully inserted between the workpiece and the tool would no longer fall. After approaching the starting point, the lathe was given a step feed of 12.7 µm before checking if the shim had already been jammed. The shim thickness was 0.76 mm. Thus, this procedure ensured that the workpiece would be some 0.76 mm from the tool cutting edge. By following this positioning methodology, the tool remained unused up to actual machining for data acquisition. The machining feed was kept constant at 50 µm/rev. The cutting speed varied from 1 m/s to 4 m/s. Each machining trial was set to 6 workpiece rotations, which implies total length of cut (π x OD x # of rotations) = 0.38 m. At the end of the machining, the feed was reversed immediately after the last forward rotation.

A data acquisition board was used in connection with computer software to record the lathe/camera trigger signal, and to record machining force as measured by a piezo-based dynamometer. The dynamometer channel used to measure the cutting force had a measuring range of -5 kN to 5 kN, resolution less than 0.01 N, linearity of ±1 % of full scale output (FSO), hysteresis less than 1 % FSO, stiffness of 0.4 kN/µm, and resonant frequency of 3.1 kHz. The dynamometer channel used to measure the thrust force had a measuring range of -5 kN to 20 kN, resolution less than 0.02 N, linearity of ±1 % FSO, hysteresis less than 1 % FSO, stiffness of 2 kN/µm, and resonant frequency of 6.3 kHz.

The upper side of the chips produced by machining was imaged using a three-dimensional (3D) profilometer with height resolution of 50 nm. The upper side is the side opposite to the one in contact with the tool, where shear localization at the primary shear plane usually results in well-defined ridges across the chip width. The tool rake face was imaged using another 3D profilometer operated at an optical resolution of 0.92 µm, to characterize tool wear (notch wear of the cutting edge) after the cutting.

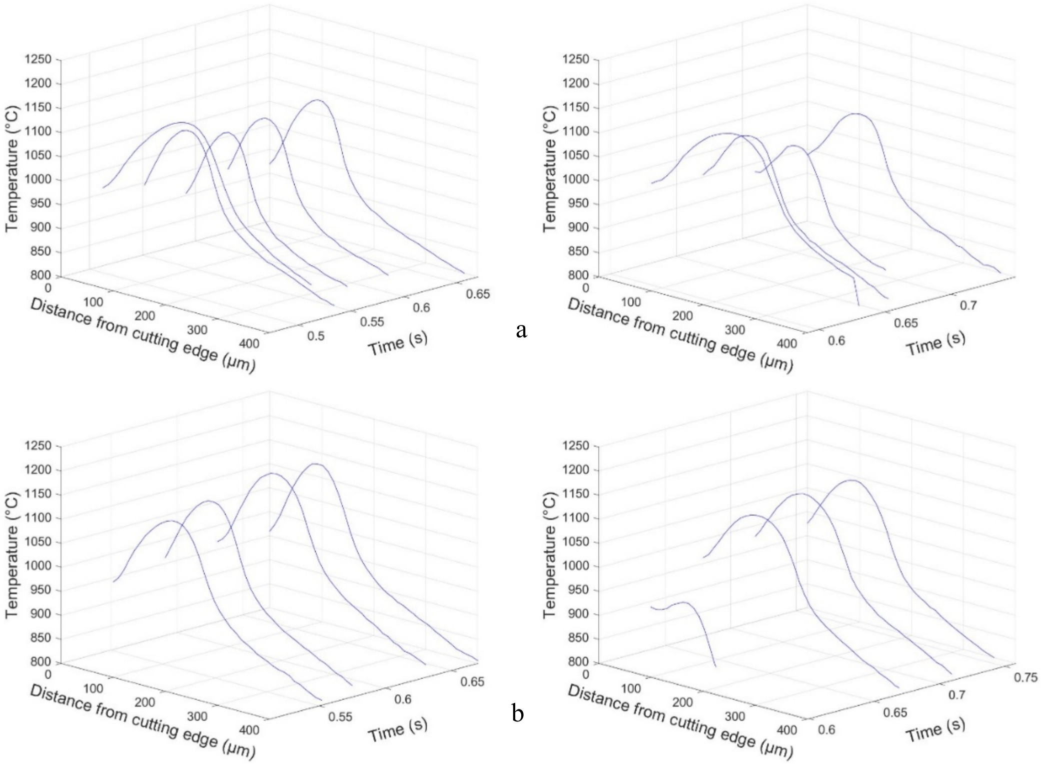

Fig. 3. Evolution of the temperature profiles throughout the machining cuts at cutting speed = 2 m/s. (a) Material: **CW IN 625**; left: trial 1, right: trial 2. (b) Material: **AM IN 625**; left: trial 1, right: trial 2.

3. Results

An example image (frame) of the radiation intensity field recorded by the camera appears in Fig. 2. This image shows the full field on the tool rake face and a reflection of it from the tool flank face. The dashed line separating the two symmetric regions in the image corresponds to the tool cutting edge. The side to the right of this line corresponds to the direct image of the rake face. The side to the left of this line corresponds to the reflection of the rake face on the flank face. The chip flows perpendicular to the dashed line towards its right side. Note that the length of the high-intensity region in Fig 2 corresponds to the full width of the workpiece. As shown in the figure, the temperature field along this width is uniform. With increasing distance from the cutting edge along the chip flow direction, however, the radiation intensity first rises and then drops. Thus, the point of maximum radiation intensity along the tool rake face is at a finite distance from the cutting edge. This behavior was observed in all machining trials from both AM IN 625 and CW IN 625, at all cutting speeds. The generic field shape makes it possible to extract mean radiation intensity profiles (i.e., radiation intensity as a function of the distance from the cutting edge). The calculation involves averaging the intensities at a given distance from the tool cutting edge over a band at the center of the cut. The radiation intensity can then be transferred into true temperature after inverting the Sakuma-Hattori equation. This calculation was performed for bands that were 100 µm to 150 µm wide (10 % to 15 % of the width of the cut).

Figure 3 shows the temperature profiles from each image (frame) from the start of the machining trial to the end. The data in the figure is for cutting speed = 2 m/s, for both the CW and the AM materials. The temperature is the vertical axis. The other two axes are distance from the cutting edge and time during the cut. Note that the cutting edge is at the origin, but time zero is not. Time zero is the start of lathe motion and image acquisition. Since lathe motion and image acquisition started simultaneously, and the trigger signal was recorded along with the force signal, it was possible to synchronize force and frame acquisition.

After performing the synchronization, the temperature (peak temperature) and machining force (cutting and thrust forces) were plotted together. The combined plots for cutting speed = 2 m/s, and for both the CW and the AM materials are shown in Fig. 4.

From Figs. 3 and 4 it is clear that both the cutting and the thrust force reached steady state within one or two rotations of the workpiece. During the initial rotations, when the temperature profile is higher than those from the rest of the cut, so is the machining force. This spike in temperature and force is probably due to the step left on the workpiece after retracting it. The spikes may be avoided by finishing the workpiece flat before the next machining trial, but for the data that is available, the cleaning procedure was not performed. The data from the first two rotations are not included in the statistics that were extracted from the measurements. The dashed vertical lines printed on the plots in Fig. 4 show the period of time from which statistics (mean temperature and machining force) were calculated. These periods are from the middle of the cutting, where temperature and machining force are relatively steady.

To extract the statistics from the temperature profiles, the mean image is calculated by averaging true temperatures, pixel by pixel, across the frames from the steady state. The standard deviation is also calculated pixel by pixel. The band corresponding to the middle of the workpiece width is identified, and the true temperature values that are at a given distance from the tool cutting edge are averaged. The standard deviation characterizing the measurement scatter is taken as the standard deviation of the mean, which is computed from both the true temperatures at a given pixel across the frames, and the true temperatures at a given distance from the cutting edge across the width of the workpiece.

The temperature profiles shown in Fig. 3 are mean profiles from the band corresponding to the middle of the workpiece. The temperatures shown in Fig. 4 are mean peak temperatures extracted directly from Fig. 3. The mean cutting and thrust forces, and the standard deviation of the cutting and thrust forces are also computed during the steady state period (from Fig. 4). These forces are projected parallel and normal to the tool rake face, and the ratio of parallel force to normal force is taken as the friction coefficient. The mean peak temperature, the distance to this mean peak temperature, the mean cutting force, the mean thrust force, the mean friction coefficient, and the corresponding standard deviations are summarized in

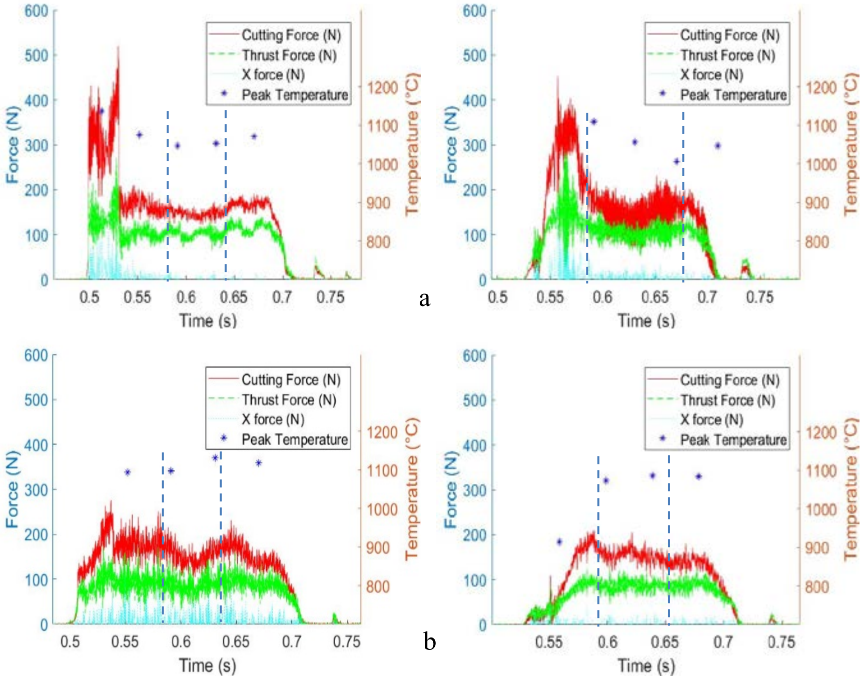

Fig. 4. Evolution of the peak temperature and the machining force throughout the cuts at cutting speed = 2 m/s. (a) Material: **CW IN 625**; left: trial 1, right: trial 2. (a) Material: **AM IN 625**; left: trial 1, right: trial 2.

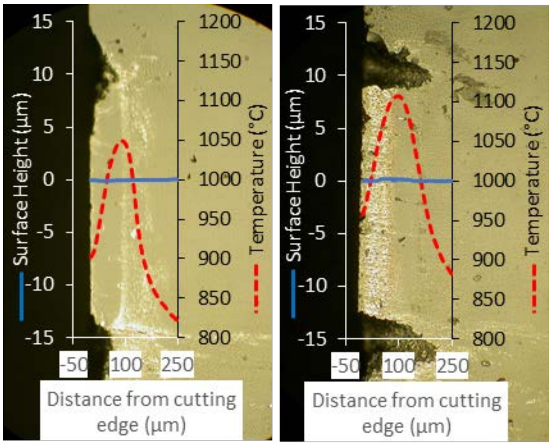

a b

Fig. 5. Wear patterns on the tool rake face after cutting at cutting speed = 2 m/s. (a) Rake face view, material: CW IN 625. (b) Rake face view, material: AM IN 625. The blue traces in “a” and “b” are the mean surface profile across the middle of the chip-tool contact width. The orange traces are the mean temperature profiles from the middle of the cut.

Table 1. The error in the distance from the cutting edge to the peak temperature is taken as the width of one pixel (10.24 µm).

Typical tool rake face wear patterns for cutting speed = 2 m/s, for both CW and AM materials are shown in Fig 5. These profiles are mean profiles from the middle of the chip-tool contact, where tool wear is minimal. The mean cutting tool volume loss for all cuts at cutting speeds from 1 m/s to 3 m/s is summarized in Table 2. The images of the chip upper sides for cutting speeds from 2 m/s to 4 m/s, and for both the CW and the AM materials are shown in Fig. 6.

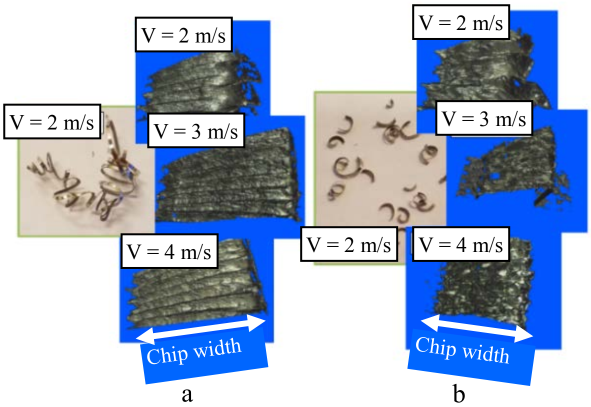

a b

Fig. 6. (a) Typical CW IN 625 chips. (b) Typical AM IN 625 chips. V = cutting speed. Tool: tungsten carbide (WC) with rake angle = 5° and relief angle = 6°. The chip width is 0.9 mm.

4. Discussion

There are significant differences between the machinability of AM IN 625 and CW IN 625. The differences are in maximum temperature at the chip-tool interface, tool wear, and chip formation.

As can be seen from Fig. 4 and Table 1, the peak temperature at the chip-tool interface during the machining of the AM material is about 16 °C , 51 °C , and 69 °C higher than that of the CW material, for cutting speeds of 1 m/s, 2 m/s, and 3 m/s, respectively. The distance from the cutting edge to the peak temperature for AM and CW materials are nearly identical. However, for both materials, this distance decreases with increase in cutting speed.

As can be seen from Table 2, the volume loss at the tool cutting edge and the rake face during the machining of the AM material is about 3, 4, and 15 times that of the CW material, for cutting speeds of 1 m/s, 2 m/s, and 3 m/s, respectively. Most of this volume loss occurs at the sides of the chip-tool contact where the lateral edges of the chip contact the tool (notch wear seen in Figs. 5 (a) and (b)). After machining the AM material, the tool cutting edge was significantly worn across the full width of chip-tool contact, for cutting speed = 1 m/s and 3 m/s. However, for cutting speed = 2 m/s, the tool cutting edges after machining both the AM and the CW materials were nearly intact (Figs. 5 (a) and (b)).

The wear makes temperature and force comparisons rather difficult, but since the tool cutting edges from both the AM and the CW materials at cutting speed = 2 m/s remained nearly intact, and the notch wear presumably has a negligible effect on temperature, temperature comparisons at this cutting speed are possible. The assumption being made is that since the tool temperature is measured between the notches on the tool rake face, it will be controlled by the contact in the middle region where little wear is observed.

The parasitic force from the significant notch wear may be a strong component of total force. Therefore, the assumption that the notches do not affect temperature cannot be extended to force. Under this assumption, the measured temperature difference between the AM and the CW materials may be explained by differences in strength, since the higher rake face temperature at cutting speed = 2 m/s for the AM material is consistent with its higher yield stress and ultimate tensile strength. Temperature and wear are intrinsically related to one another, therefore,

Table 1. Summary of temperature and force*.

Material/Machining velocity		Peak Temperature (°C)	Distance from the cutting edge to the peak temperature (μm)	Cutting Force (N)	Thrust Force (N)	Coefficient of friction
CW IN 625/ 1 m/s	Trial 1	943 ± 7	122.9 ± 10.2	172 ± 7	114 ± 6	0.54 ± 0.03
	Trial 2	943 ± 2	122.9 ± 10.2	161 ± 11	112 ± 8	0.58 ± 0.04
	Mean	943	122.9	167	113	0.56
AM IN 625/ 1 m/s	Trial 1	973 ± 2	133.1 ± 10.2	165 ± 13	108 ± 8	0.54 ± 0.05
	Trial 2	944 ± 2	133.1 ± 10.2	154 ± 12	107 ± 12	0.58 ± 0.06
	Mean	959	133.1	160	108	0.56
CW IN 625/ 2 m/s	Trial 1	1048 ± 1	92.2 ± 10.2	151 ± 11	103 ± 12	0.57 ± 0.07
	Trial 2	1042 ± 5	92.2 ± 10.2	141 ± 34	101 ± 17	0.6 ± 0.2
	Mean	1045	92.2	146	102	0.6
AM IN 625/ 2 m/s	Trial 1	1112 ± 3	112.6 ± 10.2	157 ± 22	89 ± 22	0.5 ± 0.1
	Trial 2	1079 ± 1	112.6 ± 10.2	150 ± 15	87 ± 12	0.47 ± 0.08
	Mean	1096	112.6	154	88	0.5
CW IN 625/ 3 m/s	Trial 1	1144 ± 1	81.9 ± 10.2	156 ± 14	91 ± 24	0.5 ± 0.1
	Trial 2	1059 ± 1	81.9 ± 10.2	158 ± 20	101 ± 32	0.5 ± 0.2
	Mean	1102	81.9	157	96	0.5
AM IN 625/ 3 m/s	Trial 1	1194 ± 3	71.7 ± 10.2	214 ± 29	143 ± 36	0.6 ± 0.2
	Trial 2	1147 ± 3	71.7 ± 10.2	161 ± 14	150 ± 18	0.8 ± 0.1
	Mean	1171	71.7	188	147	0.7

*The error values for peak temperature, forces and friction coefficient correspond to one standard deviation. The error value for distance to peak temperature corresponds to the distance between two adjacent pixels.

since there was tool wear throughout the experiments, it is not possible to fully isolate the effect of material strength on temperature. Since the total volume loss for AM was, for all machining trials, higher than the total volume loss for CW, it can be concluded that the AM material is more difficult to machine than the CW material. There is significant material transfer from the chip to the tool rake face for AM, but not for CW (Figs. 5 (a) and (b)). The transfer may be due to higher nitrogen content in the AM material than in the CW material, due to the nitrogen atmosphere used during the LPBF process. Metal carbo-nitrides and ternary nitrides have been observed in powder produce in a nitrogen atmosphere [23]. It is hypothesized that higher adhesion between nitrides and the ceramic tool leads to the increased deposition observed.

Table 2. Tool wear summary.

Material/Machining velocity		Volume loss per unit width (μm^2)
CW IN 625/ 1 m/s	Trial 1	228
	Trial 2	61
	Mean	145
AM IN 625/ 1 m/s	Trial 1	355
	Trial 2	514
	Mean	434
CW IN 625/ 2 m/s	Trial 1	180
	Trial 2	112
	Mean	146
AM IN 625/ 2 m/s	Trial 1	758
	Trial 2	471
	Mean	615
CW IN 625/ 3 m/s	Trial 1	N/A
	Trial 2	63
	Mean	63
AM IN 625/ 3 m/s	Trial 1	788
	Trial 2	1082
	Mean	935

As can be seen in Fig. 6, the AM IN 625 chips at all cutting speeds from 2 m/s to 4 m/s are characterized by a rather non-uniform segmentation across their width (direction parallel to the workpiece width); whereas the CW IN 625 chips show uniform segmentation across their width indicative of adiabatic shear banding. The non-uniform segmentation is likely due to shear failure initiated by microvoids, or hard second phase particles present in the rapidly solidified AM material [24], and it is consistent with its lower elongation at breakage.

As can be seen from Table 1, the mean cutting and thrust forces, and the coefficient of friction from the machining of the AM and CW materials are all within the data scatter. It is expected that tool temperature and machining force are correlated, and that the higher yield stress, ultimate tensile strength, and machining temperatures measured for the AM material should have resulted in a higher machining force. As per the measurements, it cannot be concluded that the force from the machining of the AM material is higher than that of the CW material.

5. Conclusions

From the data presented herein, it can be concluded that:

1) The peak temperatures at the chip-tool interface during the machining of AM IN 625 produced by LPBF are about 16 °C, 51 °C,

and 69 °C higher than that of the CW material of similar composition, for cutting speeds of 1 m/s, 2 m/s, and 3 m/s, respectively.

2) The distance from the cutting edge to the location of the peak temperature is nearly identical for AM and CW materials. This distance decreases with increase in cutting speed.
3) Under identical machining conditions, tool notch wear while machining the AM material is more severe than while machining the CW counterpart. Tool wear increases with cutting speed. For the YAG tool material, the tool wear for AM material, as measured from total volume loss, after about 0.4 m of cut length, is 3, 4, and 14 times higher than that for CW material.
4) There is significant material transfer from the chip to the tool rake face for AM, but not for CW IN 625. The transfer may be due to the presence of metal carbo-nitrides in the AM material.
5) The AM material produces chips that show non-uniform segmentation across the chip width, whereas the CW material produces chips that show uniform segmentation typically observed in adiabatic shear banded chips. This suggests that adiabatic shear banding may be inoperative during the machining of the AM material, probably due to second phase particles or microvoids initiating shear failure due to damage.
6) The higher temperature and wear, and the non-uniform segmentation in the machining of the AM material are consistent with the material's higher strength and lower ductility, when compared to the CW counterpart.
7) Differences in machining force for the AM and CW materials could not be resolved due to the confounding effect of tool wear in the form of notch wear at the lateral sides of the chip-tool contact.

Acknowledgements

This material is based upon work supported by the Department of Energy, National Nuclear Security Administration under Award Number DE-NA0003222. The authors wish to extend special thanks for Arvind Natarajan and Homar Lopez-Hawa for preparing some of the figures in this manuscript.

Disclaimers

(1) This report was prepared as an account of work sponsored by an agency of the United States Government. Neither the United States Government nor any agency thereof, nor any of their employees, makes any warranty, express or implied, or assumes any legal liability or responsibility for the accuracy, completeness, or usefulness of any information, apparatus, product, or process disclosed, or represents that its use would not infringe privately owned rights. Reference herein to any specific commercial product, process, or service by trade name, trademark, manufacturer, or otherwise does not necessarily constitute or imply its endorsement, recommendation, or favoring by the United States Government or any agency thereof. The views and opinions of authors expressed herein do not necessarily state or reflect those of the United States Government or any agency thereof.

(2) This document is an official contribution of the National Institute of Standards and Technology and is not subject to copyright in the USA. The National Institute of Standards and Technology does not recommend or endorse commercial equipment or materials, nor does it imply that the equipment or materials shown are necessarily the best available for the purpose.

References

[1] K. A. Lorenz, J. B. Jones, D. I. Wimpenny and M. R. Jackson, "A Review of Hybrid Manufacturing," in *International Solid Freeform Fabrication Symposium*, Austin, 2015.

[2] W. E. Frazier, "Metal Additive Manufacturing: A Review," *Journal of Materials Engineering and Performance,* vol. 23, no. 6, pp. 1917-1928, 2014.

[3] T. M. Mower and M. J. Long, "Mechanical Behavior of Additive Manufactured, Powder-Bed Laser-Fused Materials," *Materials Science & Engineering A,* pp. 198-213, 2016.

[4] G. Jacob, C. Brown, A. Donmez, S. Watson and J. Slotwinski, "Effects of Powder Recycling on Stainless Steel Powder and Built Material Properties in Metal Powder Bed Fusion Processes," National Institute of Standards and Technology, 2017.

[5] H. K. Rafi, D. Pal, N. Patil, T. L. Starr and B. E.

Stucker, "Microstructure and Mechanical Behavior of 17-4 Precipitation Hardenable Steel Processed by Selective Laser Melting," *Journal of Material Engineering and Performance,* 2014.

[6] D. H. Hollander, M. von Walter, T. Wirtz, R. Sellei, B. Schmidt-Rohlfing, O. Paar and H. J. Erli, "Structural, Mechanical and In Vitro Characterization of Individually Structured Ti–6Al–4V Produced by Direct Laser Forming," *Biomaterials,* vol. 27, pp. 955-963, 2006.

[7] T. Niendorf, S. Leuders, A. Riemer, H. A. Richard, T. Troster and D. Schwarze, "Highly Anisotropic Steel Processed by Selective Laser Melting," *Metallurgical and Materials Transactions B,* vol. 44B, pp. 794-796, 2013.

[8] T. Kitagawa, A. Kubo and K. Maekawa, "Temperature and Wear of Cutting Tools in High-Speed Machining of Inconel 718 and Ti-6Al-6V-2Sn," *Wear,* vol. 202, no. 2, pp. 142-148, 1997.

[9] M. Hokka, D. Gomon, A. Shrot, T. Leemet, M. Baker and V. T. Kuokkala, "Dynamic Behavior and High Speed Machining of Ti-6246 and Alloy 625 Superalloys: Experimental and Modeling Approaches," *Experimental Mechanics,* vol. 54, pp. 199-210, 2014.

[10] S. Kalpakjian and S. R. Schmid, Manufacturing Processes for Engineering Materials, Upper Saddle River, NJ: Prentice Hall, 2008.

[11] H. Shore, "Thermoelectric Measurement of Cutting Tool Temperatures," *Journal of the Washington Academy of Sciences,* vol. 15, no. 5, pp. 85-88, 1925.

[12] E. Herbert, "The Measurement of Cutting Temperatures," *Proceedings of the Institution of Mechanical Engineers,* vol. 110, pp. 289-329, 1926.

[13] P. K. Wright and E. M. Trent, "Metallurgical Appraisal of Wear Mechanisms and Processes on High-speed-steel Cutting Tools," *Metals Technology,* pp. 13-23, 1974.

[14] E. F. Smart and E. M. Trent, "Temperature Distribution in Tools Used for Cutting Iron, Titanium and Nickel," *INT. J. PROD. RES.,* vol. 13, no. 3, pp. 265-290, 1975.

[15] T. Menon and V. Madhavan, "Infrared Thermography of the Chip-Tool Interface through Transparent Cutting Tools," in *Proceedings of NAMRI/SME*, Detroit, 2014.

[16] J. C. Garcia-Gonzalez, W. Moscoso-Kingsley and V. Madhavan, "Tool Rake Face Temperature Distribution when Machining Ti6Al4V and Inconel 718," *Procedia Manufacturing,* vol. 5, pp. 1369-1381, 2016.

[17] J. C. Heigel, E. Whitenton, B. Lane, M. A. Donmez, V. Madhavan and W. Moscoso-Kingsley, "Infrared Measurement of the Temperature at the Tool-Chip Interface While Machining Ti-6Al-4V," *Journal of Materials Processing Technology,* vol. 243, pp. 123-130, 2017.

[18] B. Lane, E. Whitenton, V. Madhavan and A. Donmez, "Uncertainty of Temperature Measurements by Infrared Thermography for Metal Cutting Applications," *Metrologia,* vol. 50, no. 6, pp. 637-653, 2013.

[19] E. P. Whitenton, "An Introduction for Machining Researchers to Measurement Uncertainty Sources in Thermal Images of Metal Cutting," *International Journal of Machining and Machinability of Materials,* vol. 12, no. 3, pp. 195-214, 2012.

[20] M. Kobayashi, M. Otsuki, H. Sakate, F. Sakuma and A. Ono, "System for Measuring the Spectral Distribution of Normal Emissivity of Metals with Direct Current Heating," *International Journal of Thermophysics,* vol. 20, no. 1, pp. 289-298, 1999.

[21] B. Lane and E. P. Whitenton, "Calibration and Measurement Procedures for a High Magnification Thermal Camera," National Institute of Standards and Technology, Gaithersburg, 2015.

[22] F. Sakuma and S. Hattori, "Establishing a Practical Temperature Standard by Using a Narrow-band Radiation Thermometer with a Silicon Detector," in *Temperature: Its Measurement and Control in Science and Industry*, New York, 1982.

[23] M. R. Stoudt, R. E. Ricker, E. A. Lass and L. E. Levine, "Influence of Postbuild Microstructure on the Electrochemical Behavior of Additively Manufactured 17-4 PH Stainless Steel," *Journal of Materials,* vol. 69, no. 3, pp. 506-515, 2017.

[24] E. A. Lass, M. R. Stoudt, M. E. Williams, M. B.

Katz, L. E. Levine, T. Q. Phan, T. H. Gnaeupel-Herold and D. S. Ng, "Formation of the Ni3Nb delta-Phase in Stress-Relieved Inconel 625 Produced via Laser Powder-Bed Fusion Additive Manufacturing," *Metallurgical and Materials Transactions A,* vol. 48, no. 11, pp. 5547-5558, 2017.